A long term hydraulic stimulation study conducted at the Salak Geothermal field

Keita Yoshioka[a,*], Riza Pasikki[b], Jim Stimac[c]

[a]Helmholtz Centre for Environmental Research – UFZ, Leipzig, Germany
[b]Star Energy, Jakarta, Indonesia
[c]Stimac Geothermal Consulting, Santa Rosa, USA

Abstract

Awi 18-1 is an injection well drilled in the Cianten Caldera, near the western margin of the Salak (Awibengkok) reservoir in west Java, Indonesia. As the initial well injectivity was low, a long-term hydraulic stimulation was conducted to improve the permeability and establish a better connection to existing natural fractures. A geologic model of the area was built by integration of surface mapping, log and core data, and well performance information. The well penetrated pre- and post-caldera volcanics, the caldera ring fault intrusion and contact metamorphic zone, and marine sedimentary rocks. Permeability was found primarily near the caldera margin in pre-caldera lavas and ring fault intrusion along steeply dipping N to NW and NE trending fractures that were partially sealed by mineral precipitation. A geomechanical simulation model was developed from the geologic model to understand the injectivity evolution mechanisms and behaviours under different injection conditions, and also predict long term future injectivity performance. The model domain contains the completed interval of a deviated injection well (Awi 18-1) and covers the majority of microseismic events observed during the course of the stimulation. It simulates injectivity evolution using fully coupled processes of heat and mass transfers in poro-elastic media. The model was history-matched against the injection data (i.e. pressure) by calibrating rock mechanical and fracture properties. A few what-if scenarios under different operation conditions were simulated to evaluate the effects of injection pressure and temperature on the injectivity. These what-if scenario simulations indicate that both colder injection temperature and higher wellhead pressure lead to better injection efficiency. Also, the higher pressure had prolonged impacts while the colder temperature impacts are limited at the early time.

Keywords: Thermo-Hydro-Mechanical model, hydraulic stimulation, geothermal injection, Salak geothermal field

1. Introduction

The Salak (Awibengkok) geothermal field is the largest developed geothermal resource in Indonesia, currently sustaining 377MW of electrical generation [17]. It is a water-dominated, naturally fractured reservoir with benign fluid chemistry. A very large amount of produced brine is injected along the margins of the proven reservoir [3]. Reservoir modelling suggested that moving some fraction of that injection further from the main production area would improve the performance of the field by fostering expansion of the shallow steam cap of the system [14]. As part of the

*Corresponding author

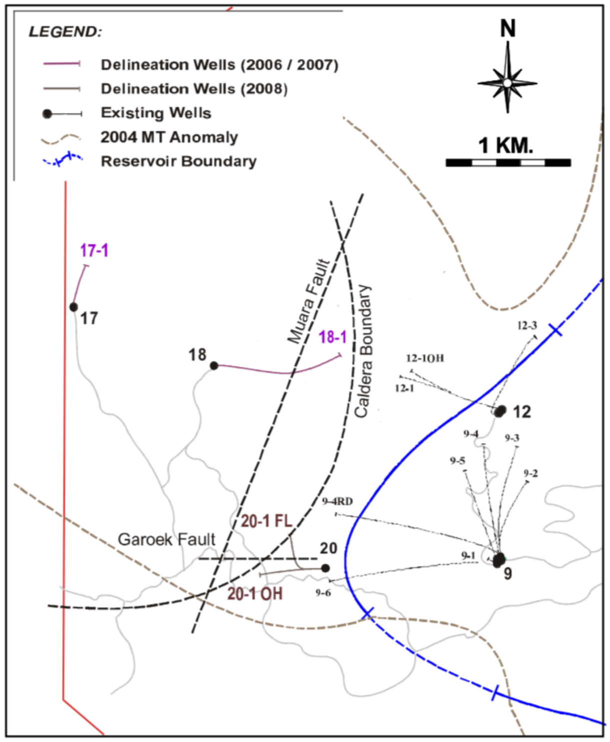

Figure 1: Map of Salak geothermal reservoir showing Awi 18-1, offset wells, and main geologic elements influencing well results in the area

effort to increase distal injection, wells were drilled to the west of the Salak field from 2006 to 2008 to delineate the potential of the area for deep injection. Awi 17-1 and 18-1 were drilled within Cianten Caldera, and Awi 20-1 was drilled just outside the inferred south-eastern caldera boundary (Fig. 1). The well permeability in this area is low, and a campaign of hydraulic stimulation was employed to improve their performance. Similar stimulation techniques have been employed elsewhere for development of Enhanced Geothermal System (EGS) such as Fenton Hill [7], Hijiori [27], Northwest Geysers [16], Soultz [31], and Desert Peak [8]. Also, attempts have been made to model the stimulation processes at these fields [6, 23, 30, 37, 43] as well as hypothetical geothermal fields [9, 21, 25, 36]. This paper describes the geologic model of the area based on the results of drilling and testing of these wells, and a geomechanical model of Awi 18-1 injectivity based on a geologic model and measured and inferred rock properties. It also summarises actual well injectivity improvement through the course of hydraulic stimulation efforts.

The Cianten caldera collapsed $\sim 670,000$ years ago, and subsequently has been partially filled with post-caldera lavas, and sedimentary deposits and tuffs [34]. Surface structures cutting post-caldera units show prominent N to NE (0-50°) and NW (330-340°) trends [33]. The Muara and Cianten faults appear to have localized erosion and eventual breaching of the caldera wall in NE, where the Cisaketi River and its tributaries now drain it and NW portion of the Salak geothermal field (Fig. 1). The caldera ring fault and the Muara fault are thought to be the most important structures based on surface exposures, and changes in rock type observed in wells. For the Muara fault, outcrop exposures and topographic scarps and breaks in slope confirm it at the surface. The exact intersection of the Muara Fault in Awi 18-1 is not known. The shallowest intersection might be at 4350-4660 ft MD where a deflection was noted in the injecting temperature log. A possible deeper intersection would be at about 6100 ft MD (2636 ft bsl) where minor permeability was indicated on the PTS log. Oblique-slip kinematic indicators were measured on the fault to the north of Awi 18-1 well. The caldera ring fault is marked by a significant scarp in some areas but has been modified by erosion in others. As described below a sequence of intrusive rocks was encountered at the expected caldera margin including both hypabyssal dacite porphyry and coarser-grained diorite. Although an increase in fracturing is observed in image logs, these structures appear to be sealed and largely impermeable based on only minor losses while drilling. The less prevalent NNW to NW and EW fractures are more common in the older rocks, however one young EW fault (Garoek Fault in Fig. 1) was observed in roadcuts near Awi 20-1. The area is thought to have a normal stress regime, with a maximum horizontal stress oriented NNE (approximately 24°).

2. Drilling and geologic constraints

Awi 18-1 was drilled with full returns, providing a good understanding of the stratigraphy and alteration encountered (Fig. 2). Additionally cores and logs were taken to provide data on fracture and rockmass properties. The well was targeted directionally to cut the caldera sequence and penetrate the eastern caldera ring fault. Based on fluid losses, drilling breaks and standpipe pressure (SPP) changes, there were minor entries observed while drilling. Partial circulation losses of 70 barrels per hour (bbls/hr) were observed from 6083 to 6115 ft MD and 6219 to 6251 ft MD. Losses of 60 bbls/hr persisted to about 6963 ft MD. Inside the caldera the well encountered a sequence of post-caldera sedimentary rocks and tuffs, caldera-related tuffs, and underlying pre-caldera andesitic to basaltic rocks that comprise the ancestral cone and underlying volcanic sequences. Submarine volcanism is evidenced by basaltic to andesitic hyaloclastite and lava interbedded with limestone and siliciclastic rocks bearing marine fossils. The caldera wall and ring dike interval were encountered from about 6000 ft MD to 7600 ft MD based on observed lithologic changes and evidence of veining and permeability. This interval consisted predominantly of hypabyssal dacite porphyry, diorite, granodiorite and contact metamorphosed marble interpreted as the caldera wall and ring dike. Protoliths of contact metamorphic rocks are mainly fossiliferous marine carbonates and tuffaceous mudstone and siltstone in some intervals. This sequence is considered to be sedimentary basement intruded by dike and sills related to caldera formation. The well exited the intrusion and contact zone at 9320 ft MD (5226 ft bsl), and reached its deepest point at 9642 ft MD (5598 ft bsl) in marine siliciclastic rocks.

The well had a conductive temperature gradient measured to about 2000 ft bsl after heat-up, similar to other far western wells (Awi 17-1, 20-1, 12-1). Nearby Awi 9 wells have convective gradients and much higher temperatures (Fig. 3).

2.1. Fracture and rock mass properties

Cores of andesitic lava and breccia, and dacite porphyry intrusion were tested for mechanical properties, and a dipole shear sonic log was also run in the 12-1/4" hole section. These data, along with complementary data from offset wells provide constraints for the geomechanical simulation. Mechanical properties estimated from well logs are listed in Table 1.

Based on resistivity formation image log (XRMI) interpretation, clusters of open and partially open steeply dipping fractures were mapped from about 3300 to 7700 ft MD, or 172 to 3902 ft bsl

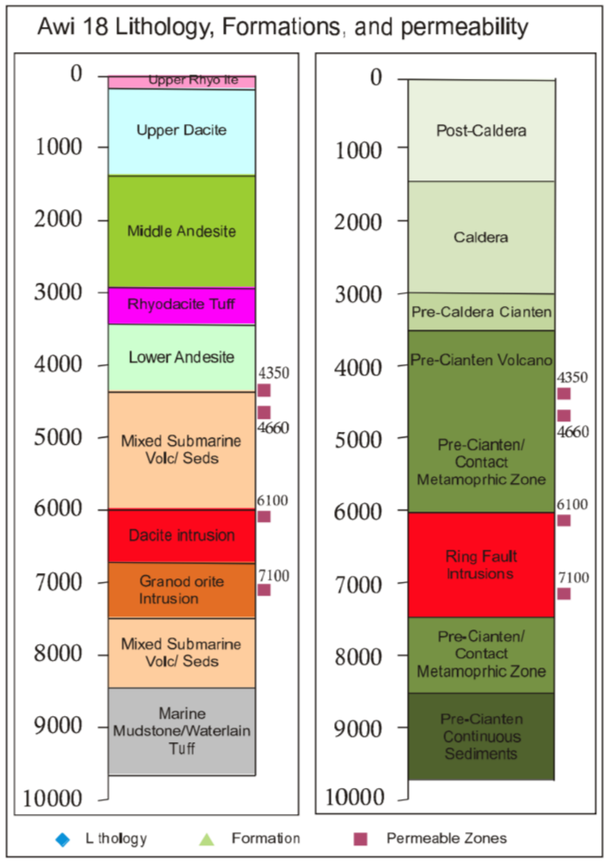

Figure 2: Awi 18-1 lithology, formations, and permeable zones.

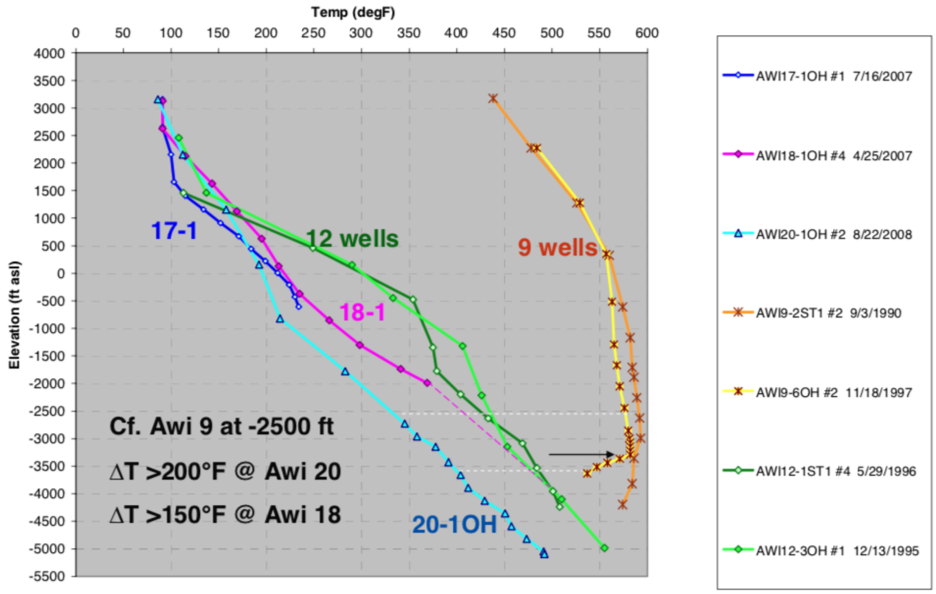

Figure 3: Static formation temperature with elevation relative to nearby wells. 9 wells represent the wells drilled from the drilling pad 9 and 12 wells from the drilling pad 12.

(Fig. 4). These fracture trends, along with fluid losses during drilling, and a PTS log described below indicate that initial permeability was primarily along NNW to NE-striking fractures (Fig. 4), favourably oriented for failure relative to current stress field.

2.2. Microseismicity

Microseismicity was associated with hydraulic stimulation at injection wellhead pressures >600 psi. The shallowest microearthquake events associated with hydraulic stimulation were at about 3600 to 3940 ft bsl (Figure 5(top)). According to [39], the average uncertainties in the location of the MEQ events were about ±208 m(682 ft) for latitude, ±281 m (922 ft) for longitude and ±362 m (1188 ft) for elevation based on statistics from the inversion software this array configuration resulted in average used. The smallest event recorded had a magnitude of -0.5M and the largest had a magnitude 2M. Events in the first phase of injection were mostly from about 1000 to 3000 m bsl (3280 to 9842 ft bsl), and in the second phase this extended further downward about about 5000 m bsl. This is deeper than the inferred permeable zones, probably due to uncertainties in the velocity model being used. However, the microearthquake locations suggest that fractures at 6100 ft MD (2636 ft bsl) or deeper were opened during the early stages of hydraulic stimulation, and that these and other fractures were stimulated at progressively deeper levels mostly in the Cianten caldera [39].

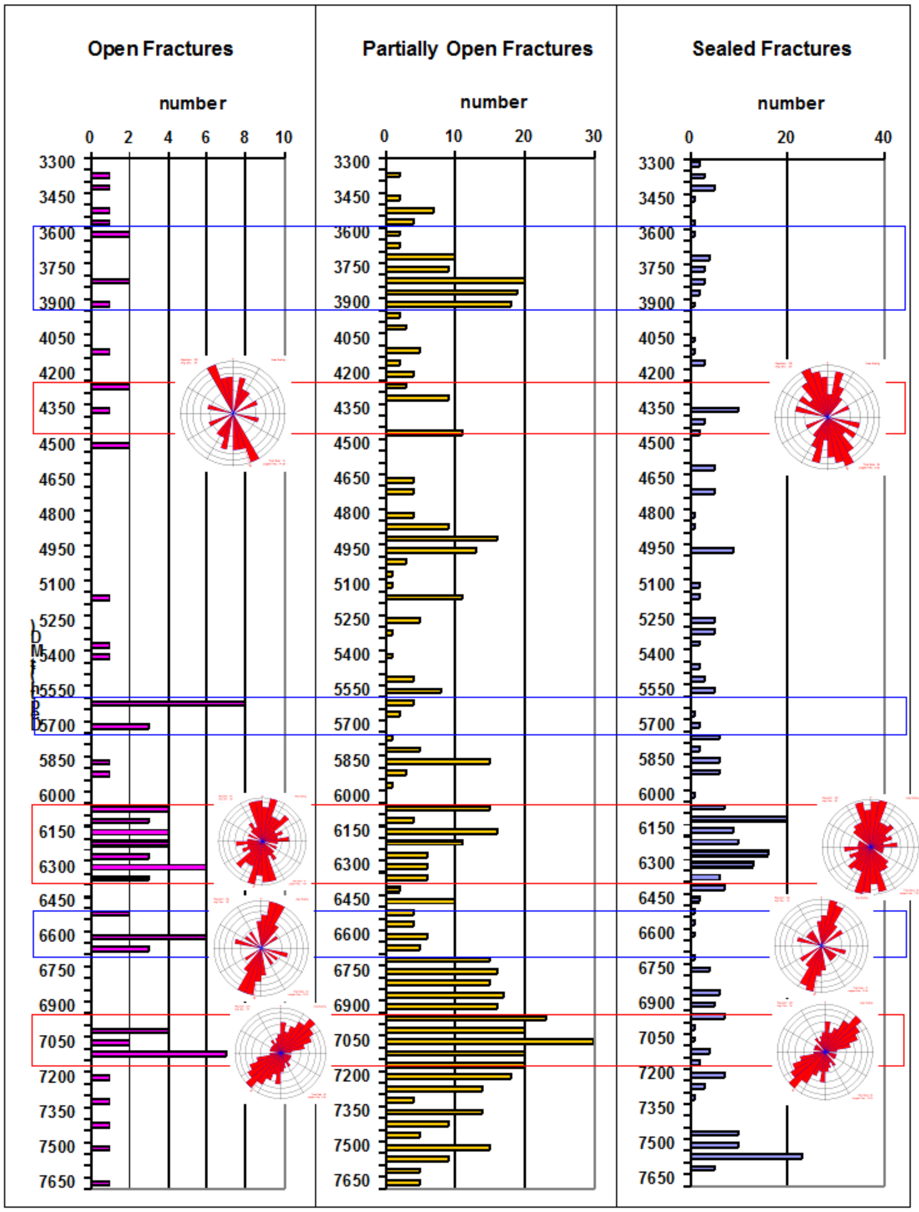

Figure 4: Histograms of fracture density with depth (50 ft intervals) and fracture strike for open and partially open (left side) and all (right side) for intervals that were modelled. Interpreted permeable zones in red boxes.

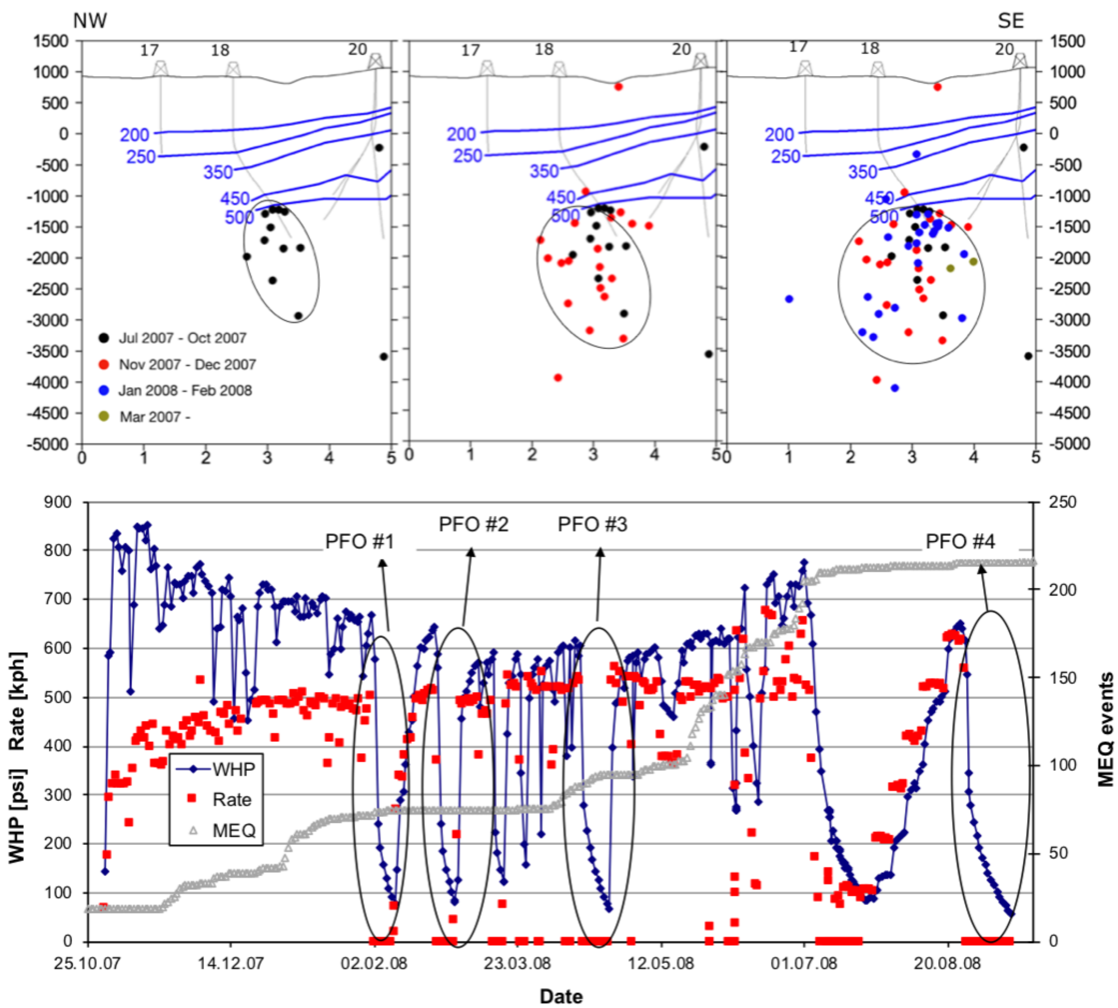

Figure 5: Cross sections of microseismic events during shutdown of injection in Awi 18-1 well (the vertical scale is in m). The blue lines are inferred temperature isotherms based on well temperature profiles in °F (top). Injection history of the phase-2 stimulation from October 2007 until August 2008. Recorded injection rates, well-head pressures, and cumulative MEQ events (bottom).

Table 1: Lithology and rock properties.

TVD ft	Lithology	Elastic modulus Mpsi	Poisson's ratio	Density g/cc
3440-4615	Andesite/Dacite	6.5	0.3	2.57
4615-4656	Basalt	8.5	0.31	2.5
4656-4730	Rhyolite	9	0.31	2.77
4730-5152	Dacite	7	0.3	2.55
5152-5352	Andesite	6	0.32	2.53
5352-5544	Limestone	5	0.32	2.58
5544-6200	Limestone w/ some dacite	7.5	0.31	2.64
6200-6965	Dacite/Andesite	9.5	0.28	2.45
6967-13440	Unknown	9.5	0.28	2.45

3. Well injection history

3.1. Pre-stimulation measurements

The well completion test, which measured the initial injectivity index (II) of Awi 18-1 of 0.45 kph/psi, was below expectations. Fig. 6 shows the results from a step-rate injection test in November 2006 shortly after the well was completed. It indicates that the II increases with the higher wellhead pressure.

The injectivity index (II) is defined as

$$\begin{aligned} \mathrm{II} &= \frac{q_{\mathrm{inj}}}{p_{\mathrm{wf}} - p_r} \\ &= \frac{q_{\mathrm{inj}}}{p_{wh} + \triangle p_h - \triangle p_f - p_r}, \end{aligned} \tag{1}$$

where q_{inj} is the injection rate, and p_{wf}, p_{wh}, and p_r are the pressure at the downhole, wellhead, and reservoir respectively. $\triangle p_h$ and $\triangle p_f$ are the hydrostatic and frictional pressure loss. The kinetic pressure loss in the pipe is generally negligible. Though downhole pressures are typically measured directly in conventional geothermal wells, here they are calculated from the wellhead pressures p_{wh} considering that the wellbore is fully filled with water during the injection tests due to the low formation permeability. Rearranging Eq. 1 gives

$$q_{\mathrm{inj}} = \mathrm{II}(p_{wh} + \triangle p_h - \triangle p_f - p_r). \tag{2}$$

From Eq. 2, the injectivity index is estimated from the slope of injection rate plot against the wellhead pressure assuming that II is constant with the injection rate, the frictional pressure loss is negligibly small and the test duration is short enough that p_r change is negligible. The formation parting or the fracture extension/propagation pressure can be found at the point where the injection rate curve changes its slope [28, 32].

As part of the completion test, a pressure-temperature-spinner (PTS) log was collected under 20 bpm injection conditions (Fig. 7). An injecting wellbore model was then constructed by matching simulated wellbore pressure and injection rate to the measured data. The analysis results suggest that 34% of the injected mass is taken at 4350-4660 ft MD and 64% of the injected mass exits below 6100 ft MD. The fracture opening pressure can be read from the injectivity test (Fig. 6)

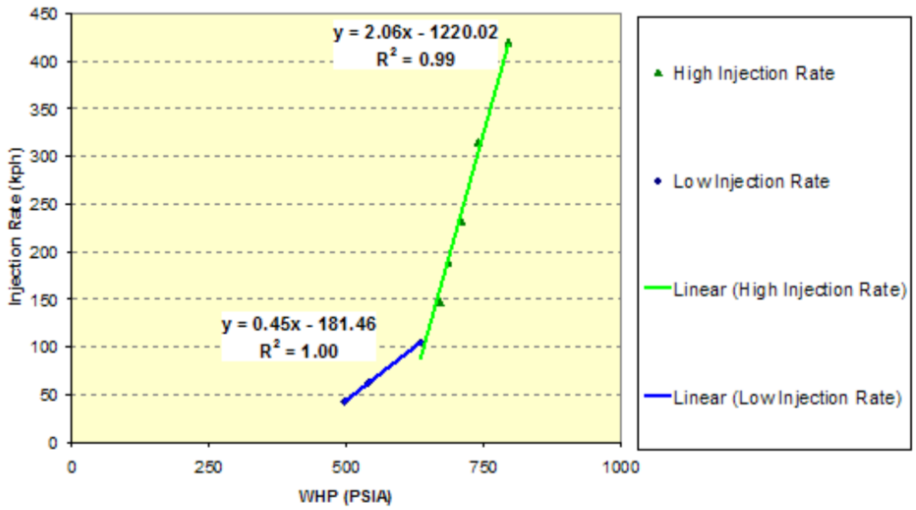

Figure 6: Injectivity test performed shortly after the well completion in November 2006.

as around 650 psi wellhead pressure. We can calculate the bottomhole pressure at 4350 ft MD applying the well pressure gradient of 0.4 psi/ft as 2390 psi ($= 650 + 0.4 \times 4350$). The minimum stress gradient of Awibengkok field is considered as 0.54 psi/ft. From this gradient, the stress at 4350 ft MD (4289 ft TVD) can be estimated as 2316 psi ($= 0.54 \times 4289$). The fracture opening pressure nearly reconciles with the least stress at this depth. On the other hand, the hoop stress ($\sigma_{\theta\theta}$) at this depth can be estimated from the so-called "Kirsch" solution ($\sigma_{\theta\theta} = 3\sigma_{\mathrm{h}} - \sigma_{\mathrm{H}}$) assuming the plane-strain condition. The lower bound for the hoop stress is obtained by using the vertical stress (maximum stress) in place of σ_{H}, which is considered as 1.04 psi/ft. Furthermore, we neglect the tensile strength of rock for a conservative estimate of the fracture initiation stress. The lowest estimate of the fracture initiation stress is then computed as 2488 psi ($= 3 \times 2316 - 4461$)[1], and it is above the hydraulic pressure achieved at this depth with the wellhead pressure of 650 psi. Therefore, it is considered that the mechanism of the injectivity improvement is attributed from stimulating the pre-existing fracture system rather than nucleating cracks in intact formation.

3.2. Long-Term water injection stimulation

After reviewing various stimulation options, long-term water injection was selected since the fracture extension pressure could be achieved with relative ease (see discussions in the previous section above). Also, thermal stresses induced by the temperature difference between the injection fluid and the formation temperature seemed sufficient to cause rock failure. As a rough estimate of the thermal impact, we consider formation of an elliptical thermal front profile around an existing fracture with the major (along the fracture) and minor (perpendicular to the fracture) axes of a_0

[1]This is, however, the lower bound. According to our estimate of the maximum horizontal stress (intermediate stress), 0.93 psi/ft, the hoop stress is estimated as 2959 psi, which makes nucleation of cracks from intact wellbore less likely at this depth.

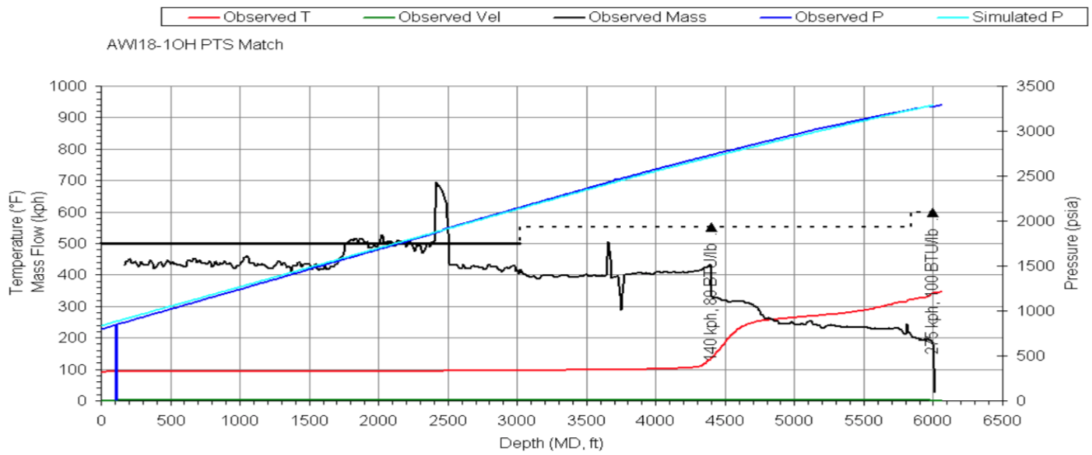

Figure 7: Pressure-Temperature spinner survey under 20 bpm and simulation by the wellbore flow model.

and b_0. From [29], the thermoelastic stress change parallel to the major axis of the ellipse (fracture) is given by:

$$\frac{\Delta\sigma}{\Delta T} = \frac{E\beta}{3(1-\nu)}\frac{1}{1+a_0/b_0}, \tag{3}$$

where σ is the total stress, E is the Young's modulus, ν is the Poisson's ratio, and the β is the volumetric thermal expansion coefficient. The elliptic thermal front profile evolves with time but given the long fracture (major axis) and slow propagation of thermal front in the perpendicular direction (minor axis), we can consider $a_0/b_0 \approx 0$. With the Young's modulus of 6 Mpsi, the Poisson's ratio of 0.28, and the volumetric thermal expansion coefficient of 1e-5/F°, the thermoelastic stress change is estimated to be 8.33 psi/F°. Referring to the example calculation in the previous section at the depth of 4289 ft TVD once more, the maximum horizontal stress is estimated as 3989 psi. If the temperature difference of 200 F° is established at this depth, then the reduced maximum horizontal stress of 2322 psi ($=3989 - 8.33 \times 200$) becomes comparable the hydraulic pressure (2390 psi) with the wellhead pressure at 650 psi.

The first phase of the injection stimulation took place from May 8 to August 8, 2007. This phase includes several water injection methods such as using a centrifugal pump with maximum rate of 1.4 bpm (29 kph), gravity flow from the power plant cooling towers with injection rates up to 3.25 bpm (68 kph), and finally with a higher capacity positive displacement pump with maximum rate of 6.7 bpm (141 kph.) At a given injection rate, the measurements from the first phase of stimulation show lower wellhead pressures than those of the post-completion injection test, which indicates that the conductivity of existing fractures improved and/or new fractures were developed around the wellbore. Given this promising result from the first phase water injection, the second phase of injection was started on October 31, 2007 using higher capacity triplex pumps. With these pumps, the injection rate can be increased up to 25 bpm (525 kph) while maintaining pressures below the 1250 psi operating limit of the current wellhead equipment. Injectate is condensate water from the power plants and its temperature at the wellhead is 90 - 100°F. The injection was stopped on August 26, 2008 and the shut-in pressures were measured until September 11, 2008. Fig. 5

(bottom) shows the whole history of injection rates and wellhead pressures during the second phase of injection stimulation.

Three pressure fall-off (PFO) tests were conducted In the course of hydraulic stimulation, and the fourth test at the end as indicated in Fig. 5 (bottom). Those data are collected to evaluate the injectivity evolution throughout the stimulation. Initially, the well accepted 418 kph (20 bpm) of injectate at 800 psi wellhead pressure and then 16 days into the second phase of injection stimulation, the wellhead pressure started decreasing. At the same time the injection rate increased and reached the maximum pump capacity after 35 days. The first PFO was started on day 95 for 7 days to evaluate further improvement of the well and changes in reservoir characteristics. The second fall-off test was conducted 15 days after the first test.

After the second PFO test, a cyclic pressure load stimulation was applied from March 14 to April 14. At the beginning of this cyclic operation, the well was put under 25 bpm (525 kph) of condensate water injection for 5 days and then put under the shut in condition for 5 days. The cycle period was gradually decreased by 1 day for the subsequent cycles until a daily pressure cycle was attained. To assess the change of well and reservoir parameters resulted from the cyclic pressure operation, the third PFO test was conducted for 10 days.

As the injection capacity of the well improved, the maximum rate from the installed triplex pumps was not sufficient to inject at pressures above the fracture extension pressure of 650 psi. The wellhead pressure under maximum pumping rate after the third PFO test stabilized at around 600 psi. An additional pump was then installed to increase the injection rate. With this configuration injection was maintained at 30 bpm (630 kph) for one month with wellhead pressures exceeding 700 psi. At the end of the stimulation program a step-rate injectivity test was conducted along with another PFO test.

For injectivity computation with Eq. 2, estimates of $\triangle p_h$, $\triangle p_f$, and p_r are necessary. When injection rate approaches to zero, p_{wh} becomes $(\triangle p_h - p_r)$. Thus we can subtract this pressure from the wellhead pressure to calculate the injectivity. However, if the liquid level falls below the wellhead, either the liquid level or the bottomhole pressure needs to be measured directly. Furthermore the reservoir pressure, p_r, may vary in the course of injection. For a better comparison, we define the injection efficiency as $I_{\text{eff}} = q_{\text{inj}}/p_{wh}$ and the resulting injection efficiency history is plotted in Fig. 8. The injection efficiency shows an increasing trend with time and improvement of injection efficiency is clearly seen in the early period while in the later times its growth becomes slower. The spikes in I_{eff} observed after well shut-ins are due to transient effects and are temporal.

Fig. 9 shows the final injectivity test result, which was taken right before the stimulation ended. The final injectivity index at wellhead pressures < 650 psi can be read from the figure as 1.26 kph/psi. Compared with the initial injectivity index of 0.45 kph/psi, it is an improvement of 180 %.

4. Injectivity analysis

4.1. Hall plot analysis

A common practice to track the injectivity evolution over time is to utilize a Hall plot [18]. A Hall plot can be constructed by plotting the integral of pressure difference between bottomhole and reservoir on the vertical axis and the cumulative injection volume on the horizontal axis. In pseudo

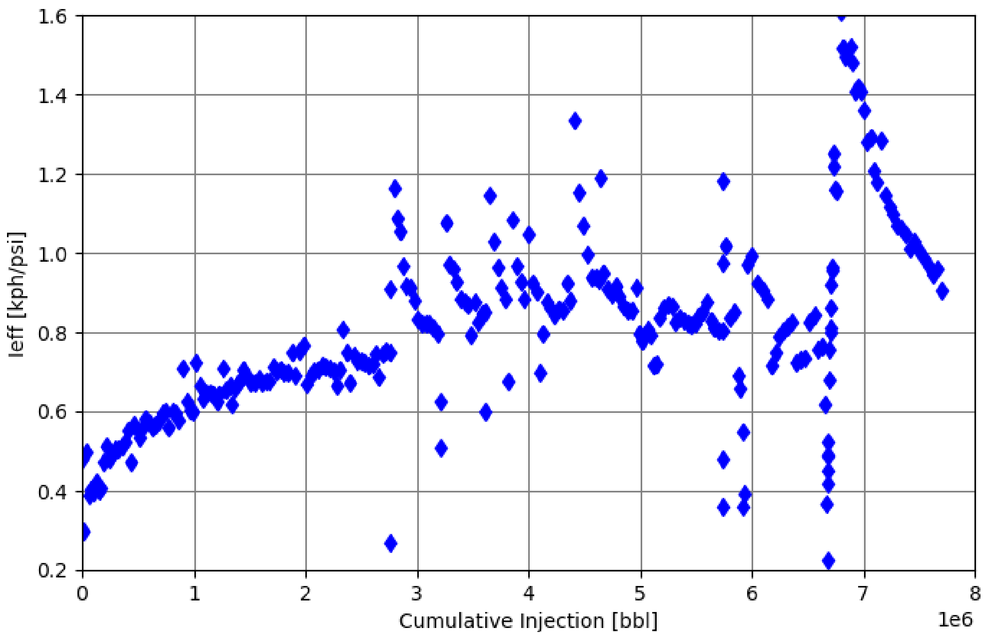

Figure 8: History of injection efficiency plotted against cumulative injection volume for the entire period of the second phase of well stimulation.

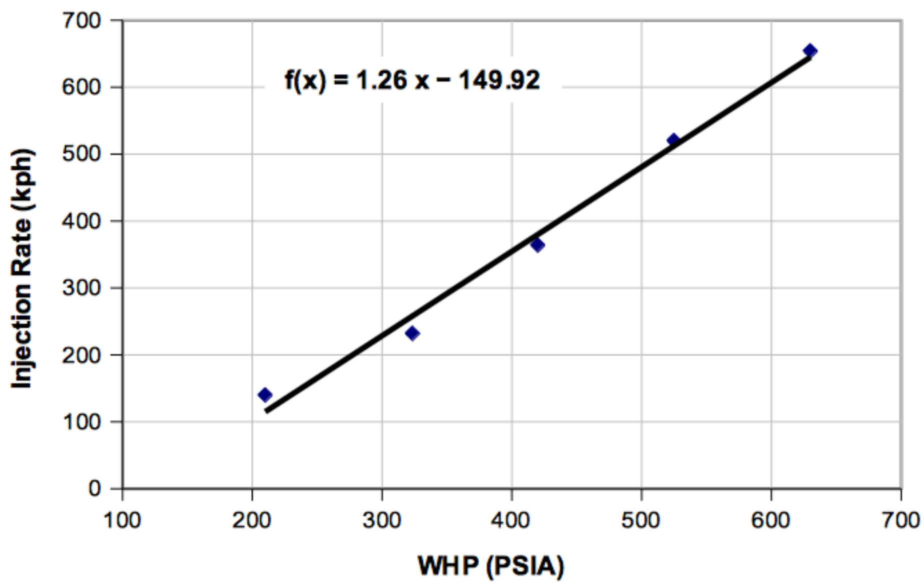

Figure 9: Injectivity test conducted after the end of the second phase stimulation.

steady state radial flow, we can write injection rate as

$$q_{\text{inj}} = \frac{2\pi kh(p_{wf} - \bar{p})}{B_w \mu \left(\ln \frac{0.472 r_e}{r_w} + s\right)}, \tag{4}$$

where k and μ are the permeability and the fluid viscosity and $\bar{p}$ is the average pressure of the reservoir. Also, B_w is the formation volume factor of the water, and h, r_e and r_w are the formation thickness, the reservoir radius and the wellbore radius respectively. Additionally, s represents the skin factor. Taking an integral on both sides, we have

$$\begin{aligned} \int_0^t q_{\text{inj}} \mathrm{d}t &= \frac{2\pi kh}{B_w \mu \left(\ln \frac{0.472 r_e}{r_w} + s\right)} \int_0^t (p_{wf} - \bar{p}) \mathrm{d}t \\ &= M \int_0^t (p_{wf} - \bar{p}) \mathrm{d}t. \end{aligned} \tag{5}$$

A plot of the cumulative injection and the integral of pressure will give a straight line with a slope of M^{-1} if the skin factor does not change with time. In Hall plot analysis, we trace slope changes of the curve. If the slope becomes steeper, that is an indication of a flow resistance development (formation plugging, wellbore scaling etc.) and if the slope becomes shallower, this would be due to a negative skin effect (fracturing, hydro-shearing etc.).

Although it is a powerful tool to monitor water injector analysis, sometimes slope changes are too subtle to detect. Izgec and Kabir [20] proposed the Hall derivative as a new diagnostic method in which the derivative is defined as

$$D_{HI} = \frac{\mathrm{d}\left(\int_0^t (p_{wf} - \bar{p}) \mathrm{d}t\right)}{\mathrm{d}\left(\ln W_i\right)}, \tag{6}$$

where $W_i = \int_0^t q_{\text{inj}} \mathrm{d}t$. Plotting a Hall integral and its derivative on the same graph aids diagnostic of the injection performance. A separation of the two curves is indicative of flow condition changes. If the derivative curve overrides the integral, it implies a skin increase. If the derivative goes below the integral, it indicates decrease in the skin. The Hall plot of Awi 18–1 is shown in Fig. 10 along with its derivative curve. Fig. 10 shows a downward separation of the Hall derivative curve from the Hall integral. The deviation of these two curves becomes wider as we inject more water, which implies that the fractures keep developing the sizes or the conductivities as more water is injected. The Hall plot is a qualitative tool but it can provide us with real-time information. We can combine its application with other techniques such as pressure fall-off test, which is discussed in the following subsection, to maximize its value.

4.2. Pressure Fall-Off test interpretation

PFO test is one of the standard pressure transient test performed to evaluate the hydraulic properties such as the conductivity, the flow regime or the flow restriction [19]. PFO like other pressure transient analyses utilizes both the pressure and pressure derivative curves and the flow characteristics are obtained by matching their absolute and relative changes. All the four PFO tests conducted (February 2 – 9, February 24 – March 1, April 14 – 24, and August 26 – September 11) are plotted in log-log scale along with the pressure derivative curves in Fig. 11. The PFO results

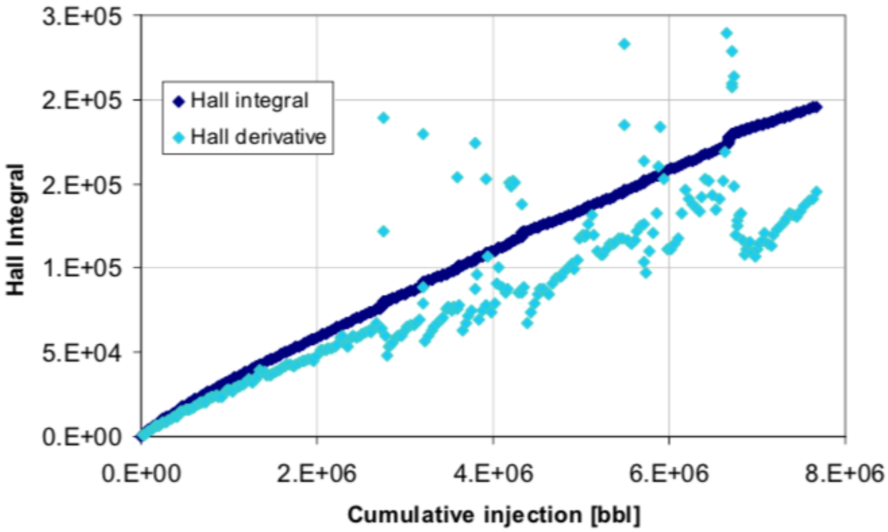

Figure 10: Derivative Hall plot.

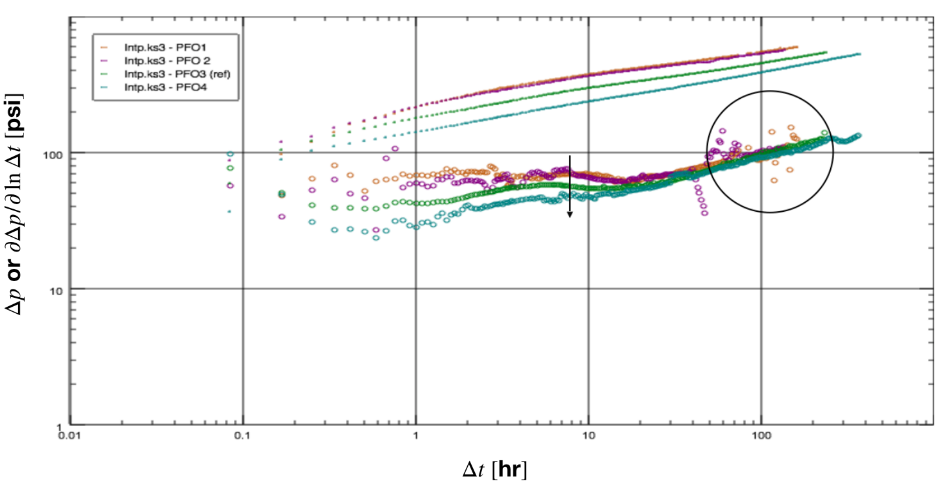

Figure 11: All four pressure fall-off tests conducted throughout the long term stimulation.

Table 2: Properties used for pressure fall-off test interpretation.

Well radius	**Pay zone**	**Porosity**	B_w	μ	Compressibility	WBS
1.02 [ft]	7000 [ft]	5%	1.08	0.2 [cp]	6.84E-6 [1/psi]	0.01 [bbl/psi]

Table 3: Summary of kh and skin estimation from pressure fall-off test interpretation

	Date	kh [md-ft]	**Skin**
PFO 1	Feb 2 – 9	6320	-2.96
PFO 2	Feb 24 – Mar 1	6180	-3.01
PFO 3	Apr 14 – 24	8280	-3.27
PFO 4	Aug 26 – Sep 11	8480	-3.73

show that the characteristics of hydraulically fractured or highly stimulated wells, which are often observed in geothermal wells [19].

From Fig. 11, two major remarks should be made. First, every test has experienced a radial flow period, as indicated by the flat derivative curves, followed by a linear flow, which is marked with a circle in Fig. 10. The distance of the radial flow region can be approximated as 600 ft away from the wellbore by matching the radial flow model to the derivative curves. The slopes of the later linear flow period are around 1/4 or slightly less as marked with a circle on Fig. 11. This is indicative of parallel sealing faults or a composite reservoir system with varying fracture fractal dimensions. This linear flow behaviour is commonly observed in fractured porous media [2] and more detailed discussion of these flow regime changes can be found in [1]. Second, the kh values in the infinite radial acting region evolve with water injection as suggested by a downward arrow in Fig. 11. In the analyses of kh and skin values, the wellbore storage was estimated based on the well configuration as 0.01 bbl/psi and is kept constant and the other fluid properties are estimated from the average pressure and temperature as listed in Table 2.

From the first PFO, kh and skin are estimated as 6320 md-ft and -2.96 respectively and the estimations from the second test are 6180 md-ft and -3.01, which is a nominal change. The second test was conducted 15 days after the first one. Although we observed some improvements in the injection efficiency history between this period (Fig. 8), these could be transient effects after the shut-in during the first PFO. The third test, which was conducted 43 days after the second test, provides kh and skin estimates of 8280 md-ft and -3.27 respectively. This is a notable improvement since the second test. Between the second and the third fall-off test, we have conducted a cyclic injection (March 14 - April 14). We have observed lower wellhead pressures ($\sim$580 psi on average) than those before the first and second tests ($\sim$660 psi). The kh and skin from the fourth fall-off test can be interpreted as 8480 md–ft and -3.73 respectively. It is not as significant a change as the one previously observed but is still a sound improvement. As we have experienced a plateau state in the injectivity after the third fall-off test, we installed the additional pump on line and also conducted a second cyclic pressure load injection. Therefore, the conductivity improvements observed in the last PFO test may be attributed either to the high injection pressure above the fracture extension pressure or the cyclic injection. All the estimation results are summarized in Table 3.

5. Numerical model

While the stimulation seems to owe its success to the longer period of injection, their quantitative impacts from the wellhead pressure and the lower injection temperature still need to be assessed. Being able to assess these impacts is of utmost importance since operating pump is one of the biggest costs and the logistics around water source has to be addressed in such long term stimulation projects. To shed light on the permeability enhancement mechanisms, a THM model capable of reproducing the permeability changes by fracture growth over the long period was built using an in-house code [10, 40]. Considering an elastic porous medium filled with a single phase fluid, following balance equations are solved.

The single phase mass balance is given as:

$$\frac{\partial}{\partial t}(\rho_f \phi) = -\nabla \cdot (\rho_f \vec{U}) + q_w, \tag{7}$$

where ρ_f is the fluid density, ϕ is the porosity, q_w is the source, and $\vec{U}$ is the darcy velociy. The darcy velocity is resolved with Darcy's law defined as:

$$\vec{U} = -\frac{K}{\mu}(\nabla p - \rho_f \vec{g}), \tag{8}$$

where K is the permeability tensor, μ is the viscosity, p is the pore-pressure, and $\vec{g}$ represents the gravity vector.

The thermal energy balance equation solved is:

$$\frac{\partial}{\partial t}\left(\rho_f C_{pf} \phi T + \rho_r C_{pr}(1-\phi)T\right) = \nabla \cdot (\rho_f h \vec{U}) - K_T \nabla^2 T + q_e, \tag{9}$$

where C_{pf} and C_{pr} are the heat capacity of fluid and rock respectively, ρ_r is the density of rock, h is the fluid enthalpy, K_T is the thermal heat conductivity, and q_e is the heat source.

These mass and the thermal energy balance are solved iteratively with the poro-thermo-elastic deformation equation. The linearised strain ε is defined as:

$$\varepsilon = \frac{1}{2}(\nabla \vec{u} + \nabla \vec{u}^{\mathrm{T}}). \tag{10}$$

The constitutive relation for a poro-thermo-elastic material reads

$$\sigma = \frac{E\nu}{(1+\nu)(1-2\nu)}\mathrm{tr}(\varepsilon)\mathbf{I} + \frac{E}{2(1+\nu)}\varepsilon - \alpha p \mathbf{I} - \frac{E}{3(1-2\nu)}\beta T. \tag{11}$$

where $\mathbf{I}$ is the second order identity tensor and α is the Biot's coefficient. The momentum balance for the total stresses is written as:

$$-\nabla \cdot \sigma = \vec{f}, \tag{12}$$

where $\vec{f}$ is the body force.

The primary variables solved from Eqs. 7, 9, and 12 are the pressure p, the temperature T, and the displacement $\vec{u}$. Eqs 7 and 9 are descretized in a finite volume scheme and Eq. 12 by a standard finite element method with hexahedral elements.

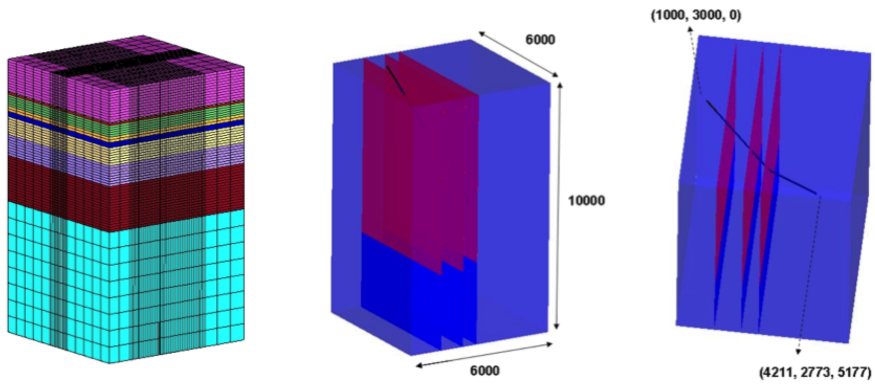

Figure 12: Computation grid with formation top and schematic of the domain.

5.1. Computational domain

As indicated in Figure 7, several clusters of open fractures were identified from logging and drilling fluid losses. The shallowest cluster can be found around 4350 ft MD which coincides with the feedzone identified from the spinner survey. From the density of the open fractures, we chose two additional zones as feedzone at 6100 ft MD and 7100 ft MD where partial losses were observed. The dominant strike of open fractures in the known well permeable zone is approximately N$\pm$30°, consistent with surface structures [33, 34]. Therefore, we consider multiple vertical fractures that intersect the deviated Awi 18-1 well in N–S direction at the 4350, 6100, and 7100 ft MD. The computational domain is extended in the vertical dimension for about 5000 ft below the well toe (about 9600 ft bsl) because the downward migration of microseismicity was observed [39]. Figure 12 shows a schematic of the computational domain.

The formation top and rock properties of the area were estimated using the log data from the Awi 18-1 well, log-based correlations for rock properties, and laboratory measurements on the core samples. As the log data are only available up to 7624 ft MD, the same properties as the last known lithology (Dacite/Andesite) are assigned in the section below this depth. All the rock mechanical properties estimated from logs are listed in Table 1.

5.2. Fracture conductivity

A relationship between fracture conductivity and applied stress has been studied extensively [13, 15, 35, 38] and also equivalent hydraulic properties for continuum representation with multiple fractures have been investigated both analytically [5, 12, 26, 41] and numerically [4, 11, 22, 24, 42]. The fractures or the zones of fractures intersected by the injection well are assumed to be near vertical and are treated as vertical high permeable zones, considering nearly identical maximum and intermediate estimated stresses in the field ($\sigma_v = 1.04$ psi/ft,$\sigma_H = 0.93$ psi/ft, $\sigma_h = 0.54$ psi/ft). The hydraulic conductivities of these fractures are updated during the non-linear iterations as a function of the effective normal stress, which is a function of the pore pressure and temperature, by applying the Gangis bed of nails model as:

$$w = w_o \left\{ 1 - \left(\frac{\sigma_N - p}{E_{eff}} \right)^{1/n} \right\} \tag{13}$$

where σ_N is the normal stress applied to the fracture face and p is the fluid pressure in the fracture. E_{eff} is the effective Youngs modulus defined as

$$E_{eff} = EA_r/A \tag{14}$$

where A is the area of the fracture face and A_r is the area of nail surfaces. Thus the fracture width is subject to the pore-pressure and the normal stress applied on the fracture. Then coupling with the fluid flow is achieved through a modification of the fracture permeability using Reynolds flow $k = w^2/12$.

As we inject cold water into the fracture system, the stress profiles of the field will be disturbed from the in-situ condition. As a consequence, a region of tensile stress around the originally dedicated fracture zones will be developed. To account for such secondary fracture propagation, elements undergoing a simple failure criterion ($\sigma_{min} - p < \sigma_t$), where σ_t is the tensile strength, are marked as failed and then the formation permeability is altered accordingly using the stress dependent permeability model for fractured media by Zhang et al. [41] based on a sugar cube type fracture geometry. The permeability change due to the aperture increment is then given by

$$k_k = k_{ko} \left(1 + \frac{\triangle b_i}{b_i} + \frac{\triangle b_j}{b_j} \right)^3, \tag{15}$$

where b is the fracture aperture and subscripts i, j, and k denote the reference coordinate. The displacement changes in each direction can be estimated by Hookes law. Therefore, in terms of stress changes, and rock and fracture stiffness, Eq. 15 can be rewritten as

$$\begin{aligned} k_k = k_{ko} \Bigg[1 &- \left(\frac{1}{K_{ni}} + \frac{b_i}{K_{ni} s_i} + \frac{b_i}{E} \right) \{ \triangle\sigma_i - \nu \left(\triangle\sigma_j + \triangle\sigma_k \right) \} \\ &- \left(\frac{1}{K_{nj}} + \frac{b_j}{K_{nj} s_j} + \frac{b_j}{E} \right) \{ \triangle\sigma_j - \nu \left(\triangle\sigma_i + \triangle\sigma_k \right) \} \Bigg]^3 \end{aligned}$$

where K_n and K_s are the fracture stiffness in the normal and the shear directions respctively, and s is the spacing between the fractures. Taking into account only the changes of the least stress, we have

$$k_k = k_{ko} \left[1 - \eta \triangle\sigma_{min} \right]^3 \tag{16}$$

where

$$\eta = \left(\frac{1}{K_{ni}} + \frac{b_i}{K_{ni} s_i} + \frac{b_i}{E} \right) + \left(\frac{1}{K_{nj}} + \frac{b_j}{K_{nj} s_j} + \frac{b_j}{E} \right) \nu$$

The "failure" of rock is not explicitly treated in the deformation. The tensile stress is allowed to further develop and no plastic strain is induced. The stress difference is then defined as the difference between the current stress and the tensile strength. We apply the bed of nails model to

Table 4: Calibrated parameters

n	A_r/A	w_o	k_o	η	σ_T
10	0.1	0.012 in	2500 md	0.005 psi^{-1}	200 psi

the prescribed fractured zones (primary fracture) and then the stress dependent permeability model was used to further expand the enhanced permeability region beyond the pre-existing fractures (secondary "fracture"). In the presented stress – permeability models, we have six calibration parameters (w_o, n, A_r/A , k_o, σ_T and η) to be determined by matching the field injection history data.

5.3. History match

The injection rate and pressure data have been monitored continuously for the entire 300 days of injection history. As calibration parameters, we have the parameters controlling primary fracture conductivity changes (Eq. 13) and secondary "fracture" (enhanced permeability) propagation (Eq. 16). Additionally, the dimensions for the primary fractures need to be prescribed. The history match has been conducted manually by calibrating the parameters. Firstly, we adjusted the parameters of the primary fractures and their dimensions, obeying the early period of the history because they are the dominant parameters in the early period before secondary fractures are developed. As spinner data below 6100 ft are not available, no information on the water allocation to each feedzone below this depth exists. Thus, the same calibration parameters and dimensions are assumed for all the feedzones. Even though assigned parameters and dimensions are the same, each fracture is allowed to behave differently as rock mechanical properties differ. The calibrated parameters are listed in Table 4 and the final history match results are shown in Figure 13. The ratio of the effective elastic module to the intact module found here (0.1) is a reasonable magnitude compared to other analyses (e.g. [42]) and the high compressibility of the fractured media (0.005 psi^{-1}) is also within the expectation. We acknowledge that the set of parameters identified here may be local minimum and there could be another combination that fits the history as well. However, this falls into an open-ended problem in the reservoir engineering community, which is beyond scope of our current study.

The overall pressure response agrees quite well and captures closely most of the features of the history. The pressure profiles of x and y planes during the simulation are shown in Figure 14. The x plane is located at the deepest feed zone (7100 ft MD) and contains the prescribed fracture, and the y-plane is at y=3000 ft. Due to the well deviation and the initial primary fracture dimension, the pressure profiles show asymmetric behaviour. Figure 15 shows the temperature profiles, which follow the fluid flow but lag from it. Figure 16 shows the permeability multiplier profiles, the enhanced permeability region propagates preferentially in the limestone layer whose elastic modulus is relatively lower and vertically along the well deviation. This flow pattern can be confirmed in the temperature profiles in Figure 15 as well. Overall, the region whose permeability is enhanced grew as more water was injected.

6. Optimal stimulation design

While one of the study's objectives is to understand the injectivity evolution mechanism and behaviour during the hydraulic stimulation, the other objective is to forecast injectivity behaviour

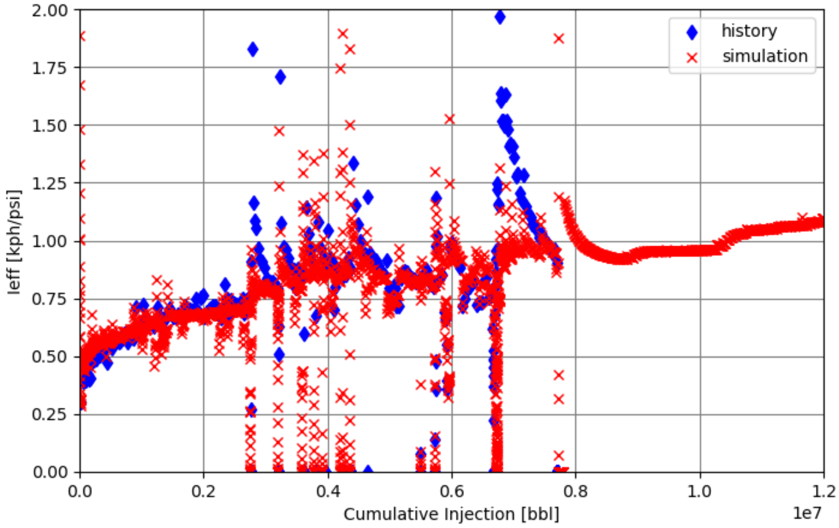

Figure 13: History match results. Injection efficiency from the history-matched model is compared against the measured data.

under possible operational situations. In this section, a couple of operational scenarios are tested.

6.1. Injection pressure

A pressure of 500 psi can be maintained from the sump gravity at the wellhead without using pumps. To investigate the efficiency, the future performances with the calibrated model considering the wellhead pressure of 500 psi, 750 psi, and 1000 psi were simulated. Figure 17 compares the injection efficiencies from these cases.

The injection efficiencies of the wellhead pressure 500 psi and 750 psi are fairly close despite the additional energy dedicated for the 750 psi case. However, with the wellhead pressure of 1000 psi, it shows steadily higher injection efficiencies than other scenarios and is projected to increase with time as the sufficient pressure to promote the permeability enhancement is provided. Of course, this argument is based on the assumption that the pore pressure will not be built up over time because of compartmentalisation or flow restrictions. As far as our long term stimulation experiment is concerned, no pronounced pore pressure build-up has been observed in the duration of the injection.

6.2. Injection temperature

As thermal contraction reduces the sub-surface stresses, colder injection water is expected to enhance the formation permeability further. During the hydraulic stimulation, we injected the condensate water from the power plant which is about 100°F. In order to decide whether we need to keep utilizing condensate water, injection performances with water temperatures of 100°F, 220°F, and 340°F were compared (Figure 18) while the wellhead pressure was set to 500 psi.

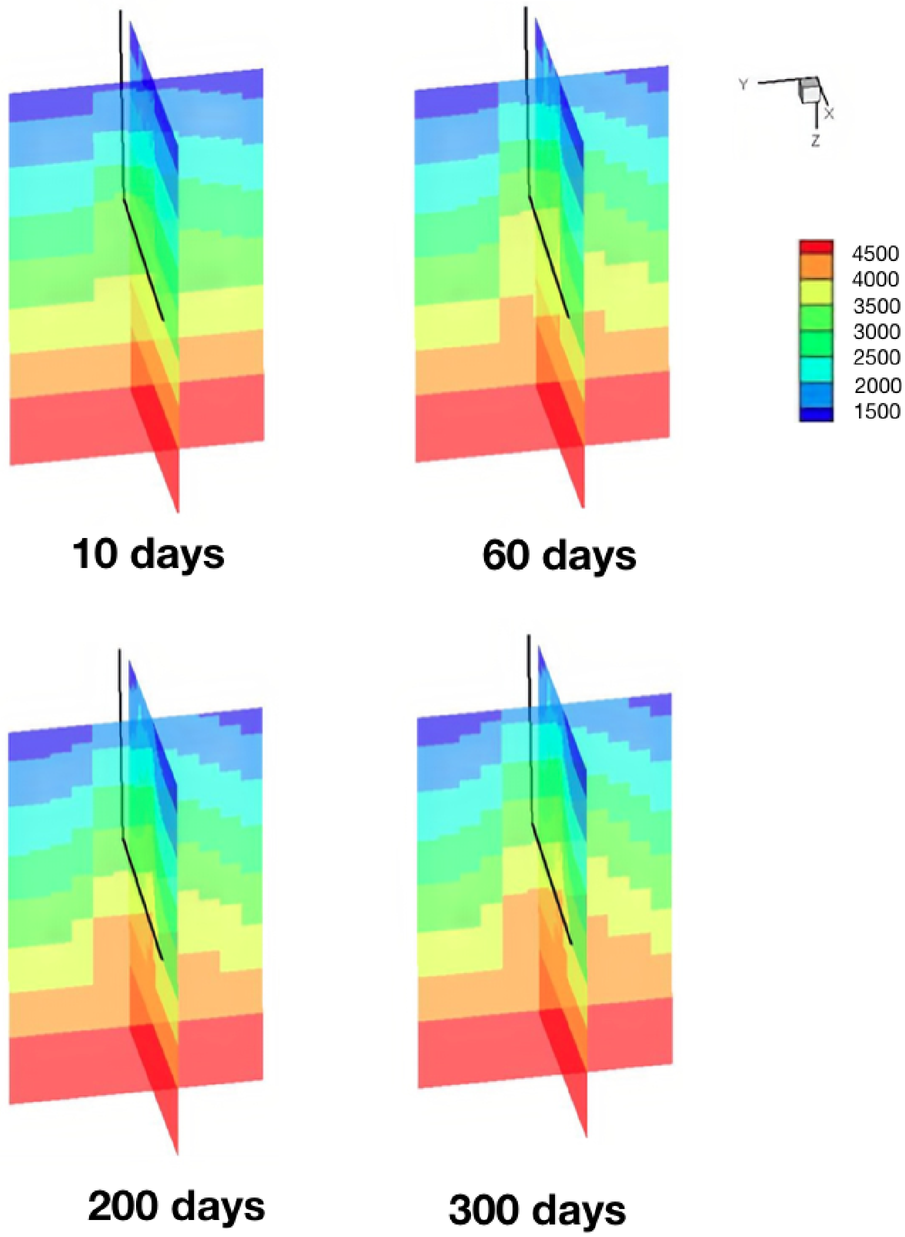

Figure 14: Snap shots of the pressure profile on the x-plane (7100 ft MD) and the y-plane (y=3000 ft) at four different times as indicated. The black line indicates the trajectory of the wellbore.

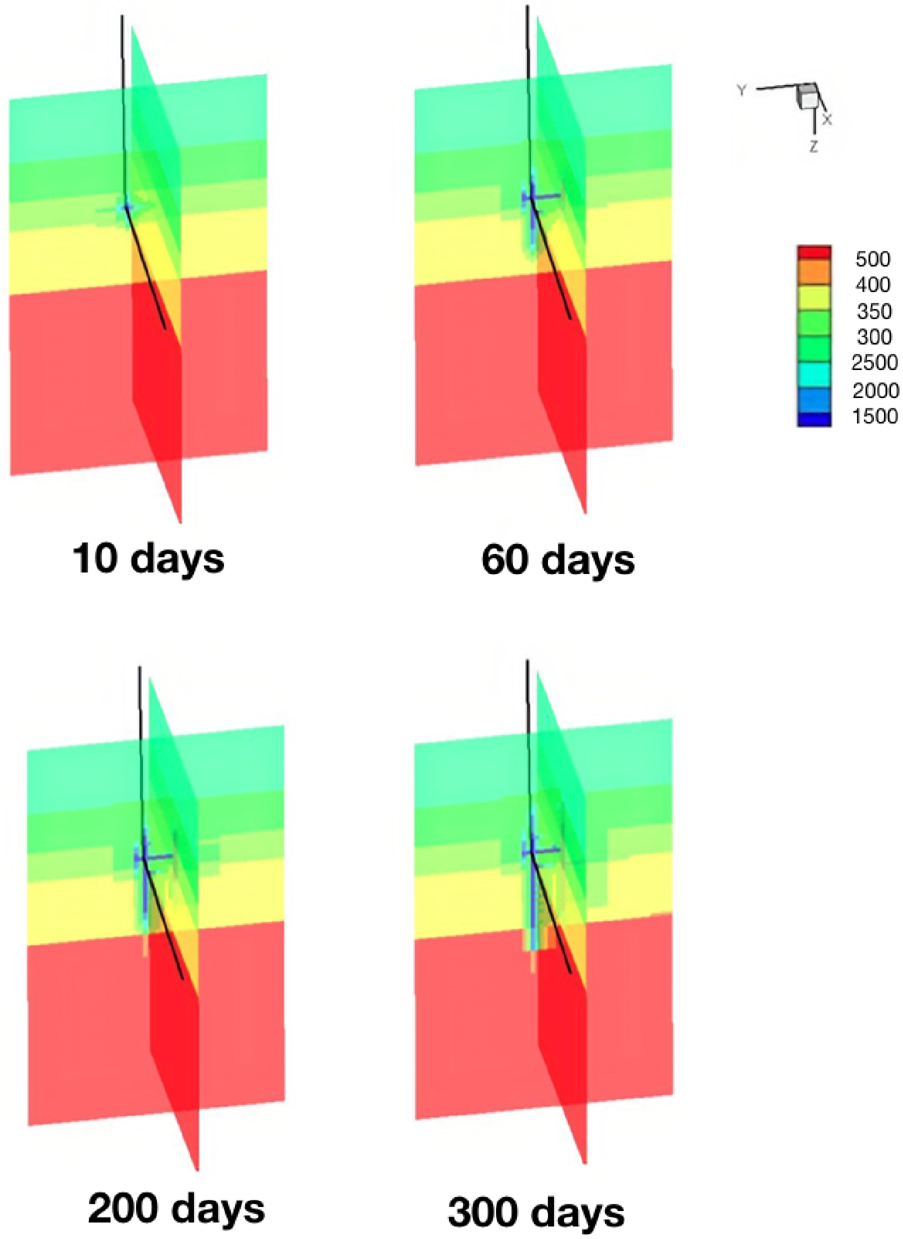

Figure 15: Snap shots of the temperature profile on the x-plane (7100 ft MD) and the y-plane (y=3000 ft) at four different times as indicated. The black line indicates the trajectory of the wellbore.

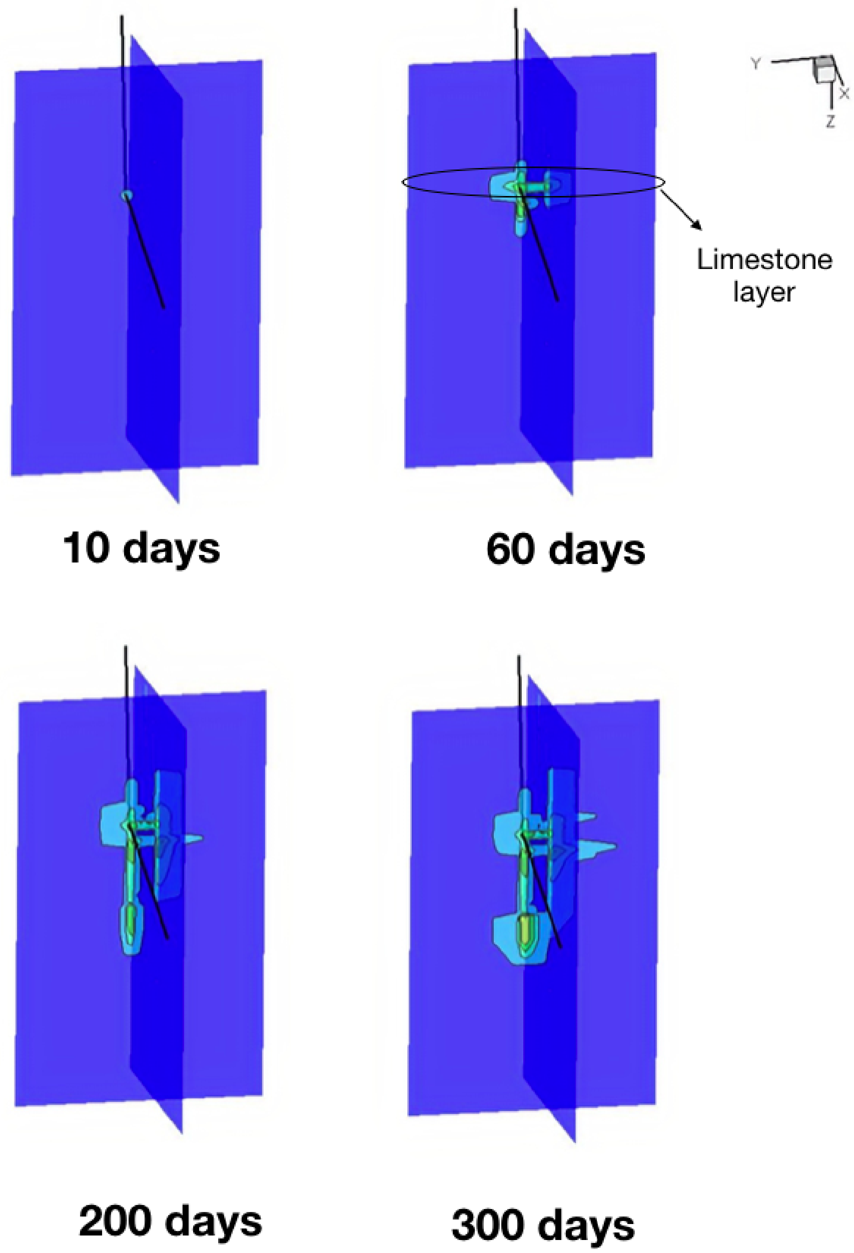

Figure 16: Snap shots of the permeability multiplier profile on the x-plane (7100 ft MD) and the y-plane (y=3000 ft) at four different times as indicated. The black line indicates the trajectory of the wellbore.

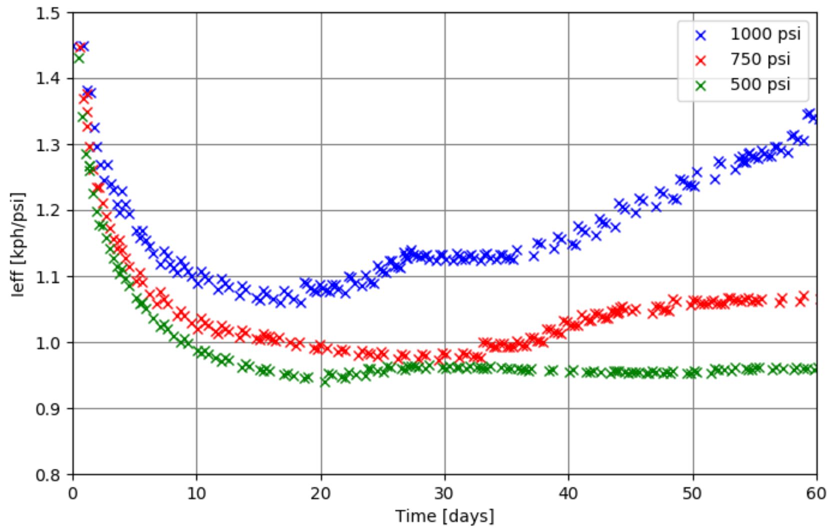

Figure 17: Future injection prediction of different wellhead pressures.

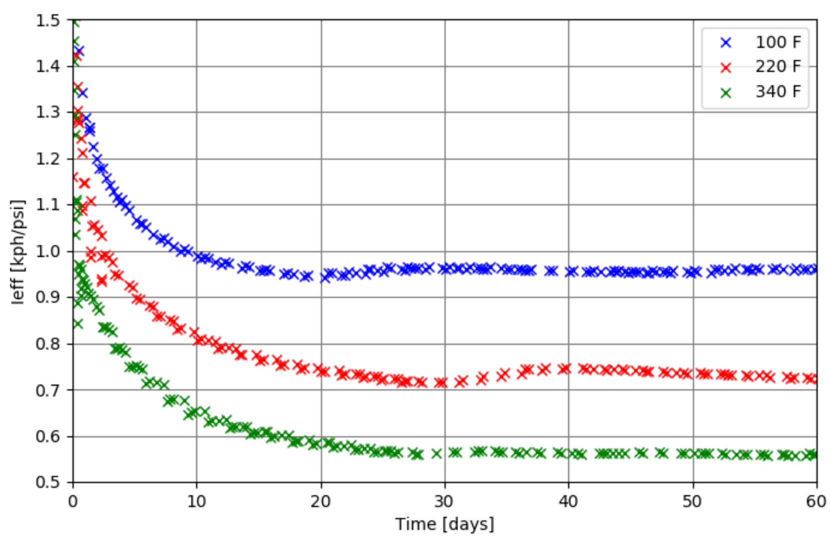

Figure 18: Future injection prediction of different injection temperatures.

The comparison results clearly show the benefits of applying lower injection temperature. The colder injection temperature is, the better injection efficiency is achieved in general with the same wellhead pressure, which indicates that the colder injection fluid can save the required wellhead pressure for sustainable water injection. Also, it can be observed from this study that unlike the high pressure case (1000 psi), the injection efficiency plateaus rather quickly. It is because the propagation of thermal front is very slow, the thermo-elastically stimulated region is limited to the close proximity from the injection well and further expansion seems to be stalled.

7. Conclusions

In this study we have conducted long-term cold water injection as a means of stimulation for a geothermal injector. To evaluate the injection performance in real-time, we applied the modified Hall method. The Hall plot analysis provides us with qualitative injectivity response which indicate development of fractures in the formation. The evolution of injectivity improvements were also assessed by periodic pressure fall-off tests. In order to better understand the injectivity evolution mechanisms, assess the prognosis of the injectivity, and develop a way forward strategy, a 3D geomechanical model of a deviated injector was built, which contains prescribed fracture planes identified from PTS and image logs. In the simulation, injectivity evolution mechanisms are considered to be twofold: 1) hydraulically dilating existing fracture apertures, and 2) creating tensile fractures (thermal cracking or spalling) from the existing fractures. The developed model was successfully calibrated against the field history and a couple of what-if operational scenarios were run. From this study, the following conclusions can be drawn:

- The higher injection pressure or the colder injection temperature, the better injection efficiency can be achieved.
- While the benefits of colder injection temperature are substantial at an early stage, the impacts will plateau eventually since its impact is slow to propagate from a localised proximity to the injection.
- If a continuing injection efficiency improvement is desired, a higher wellhead pressure needs to be applied accordingly.

8. Acknowledgements

The authors are grateful to Star Energy for permission to publish this work. Anonymous reviewers are thanked for comments and suggestions that helped improve and clarify this manuscript.

[1] J. A. Acuña. Analysis of Pressure Transient Response for an Injector under Hydraulic Stimulation at the Salak Geothermal Field , Indonesia. *Proceedings World Geothermal Congress 2010*, (April):25–29, 2010.

[2] J. A. Acuña, I. Ershaghi, and Y. C. Yortsos. Practical Application of Fractal Pressure-Transient Analysis in Naturally Fractured Reservoirs. *SPE Formation Evaluation*, 24:173–179, 1995.

[3] J. A. Acuña, J. Stimac, L. Sirad-Azwar, and R. G. Pasikki. Reservoir management at Awibengkok geothermal field, West Java, Indonesia. *Geothermics*, 37(3):332–346, 2008.

[4] A. Baghbanan and L. Jing. Stress effects on permeability in a fractured rock mass with correlated fracture length and aperture. *International Journal of Rock Mechanics and Mining Sciences*, 45(8):1320–1334, 2008.

[5] M. Bai, F. Meng, D. Elsworth, and J. C. Roegiers. Analysis of stress-dependent permeability in nonorthogonal flow and deformation fields. *Rock Mechanics and Rock Engineering*, 32(3):195–219, 1999.

[6] S. Benato and J. Taron. Desert Peak EGS: Mechanisms influencing permeability evolution investigated using dual-porosity simulator TFReact. *Geothermics*, 63(September 2010):157–181, 2016.

[7] D. W. Brown. Hot dry rock geothermal energy: important lessons from Fenton Hill. *Proceedings of the Thirty-Fourth Workshop on Geothermal Reservoir Engineering, Stanford University, CA*, pages 3–6, 2009.

[8] E. Chabora, E. Zemach, P. Spielman, P. Drakos, S. Hickman, S. Lutz, K. Boyle, A. Falconer, A. Robertson-Tait, N. C. Dacatzes, P. Rose, E. Majer, and S. Jarpe. Hydraulic stimulation of well 27-15, Desert Peak geothermal field, Nevada, USA. *Thirty-Seventh Workshop on Geothermal Reservoir Engineering*, page 13, 2012.

[9] S. De Simone, V. Vilarrasa, J. Carrera, A. Alcolea, and P. Meier. Thermal coupling may control mechanical stability of geothermal reservoirs during cold water injection. *Physics and Chemistry of the Earth*, 64:117–126, 2013.

[10] R. H. Dean and J. H. Schmidt. Hydraulic-Fracture Predictions With a Fully Coupled Geomechanical Reservoir Simulator. *SPE Journal*, 14(04):707–714, 2009.

[11] D. Dempsey, S. Kelkar, N. Davatzes, S. Hickman, and D. Moos. Numerical modeling of injection, stress and permeability enhancement during shear stimulation at the Desert Peak Enhanced Geothermal System. *International Journal of Rock Mechanics and Mining Sciences*, 78:190–206, 2015.

[12] D. Elsworth and J. Xiang. A reduced degree of freedom model for thermal permeability enhancement in blocky rock. *Geothermics*, 18(5-6):691–709, 1989.

[13] J. E. Gale. The effects of fracture type (induced versus natural) on the stress-fracture closure-fracture permeability relationships. page 9, 1982.

[14] N. Ganefianto, J. Stimac, L. S. Azwar, .R Pasikki, M. Parini, E. Shidartha, A. Joeristanto, G. Nordquist, and K. Riedel. Optimizing Production at Salak Geothermal Field, Indonesia, Through Injection Management. *Proceedings World Geothermal Congress*, (March 2005):1–7, 2010.

[15] A. F. Gangi. Variation of Whole and Fractured Porous Rock Permeability with Confining Pressure. *Int J. Rock Mech & Mining Sci*, 15(3):249–257, 1978.

[16] J. Garcia, C. Hartline, M. Walters, M. Wright, J. Rutqvist, P. F. Dobson, and P. Jeanne. The Northwest Geysers EGS Demonstration Project, California: Part 1: Characterization and reservoir response to injection. *Geothermics*, 63:97–119, 2015.

[17] G.U. Golla, T. Julinawati, R.P. Putri, G.A. Nordquist, F.T. Libert, and A.R. Suminar. The salak field, indonesia: On to the next 20 years of production. *Geothermics*, (this issue), 2019.

[18] H. N. Hall. How to Analyze Waterflood Injection Well Performance. *World Oil*, (October):128–130, 1963.

[19] R. N. Horne. *Modern Well Test Analysis.* Petroway Inc., 1995.

[20] B. Izgec and C. S. Kabir. Real-Time Performance Analysis of Water-Injection Wells. (February):116–123, 2009.

[21] P. Jeanne, J. Rutqvist, and P. F. Dobson. Influence of injection-induced cooling on deviatoric stress and shear reactivation of preexisting fractures in Enhanced Geothermal Systems. *Geothermics*, 70:367–375, 2017.

[22] M. Ki-Bok, J. Rutqvist, C.-F. Tsang, and L. Jing. Stress-dependent permeability of fractured rock masses: A numerical study. *International Journal of Rock Mechanics and Mining Sciences*, 41(7):1191–1210, 2004.

[23] T. Kohl and T. Mégel. Predictive modeling of reservoir response to hydraulic stimulations at the European EGS site Soultz-sous-Forêts. *International Journal of Rock Mechanics and Mining Sciences*, 44(8):1118–1131, 2007.

[24] J. P. Latham, J. Xiang, M. Belayneh, H. M. Nick, C.-F. Tsang, and M. J. Blunt. Modelling stress-dependent permeability in fractured rock including effects of propagating and bending fractures. *International Journal of Rock Mechanics and Mining Sciences*, 57:100–112, 2013.

[25] H. Lei, T. Xu, and G. Jin. TOUGH2Biot - A simulator for coupled thermal-hydrodynamic-mechanical processes in subsurface flow systems: Application to CO2geological storage and geothermal development. *Computers and Geosciences*, 77:8–19, 2015.

[26] J. Liu, D. Elsworth, and B. H. Brady. Linking stress-dependent effective porosity and hydraulic conductivity fields to RMR. *International Journal of Rock Mechanics and Mining Sciences*, 36(5):581–596, 1999.

[27] I. Matsunaga, H. Niitsuma, and Y. Oikawa. Review of the HDR Development at Hijiori Site, Japan. *Proceedings of the World Geothermal Congress 20052*, (April):1–5, 2005.

[28] K. G. Nolte. Principles for fracture design based on pressure analysis. *SPE Production Engineering*, 3(01):22–30, 1988.

[29] T.K. Perkins and J.A. Gonzalez. The Effect of Thermoelastic Stresses on Injection Well Fracturing. *Society of Petroleum Engineers Journal*, 25(01):78–88, 1985.

[30] J. Rutqvist, P. Jeanne, P. F. Dobson, J. Garcia, C. Hartline, L. Hutchings, A. Singh, D. W. Vasco, and M. Walters. The Northwest Geysers EGS Demonstration Project, California Part 2: Modeling and interpretation. *Geothermics*, 63:120–138, 2015.

[31] E. Schill, A. Genter, N. Cuenot, and T. Kohl. Hydraulic performance history at the Soultz EGS reservoirs from stimulation and long-term circulation tests. *Geothermics*, 70(April):110–124, 2017.

[32] P. Singh and R. G. Agarwal. Two-Step Rate Test: New Procedure for Determining Formation Parting Pressure. *JPT*, (January):84–90, 1990.

[33] J. Stimac, M. Baroek, A. Suminar, and B. Sagala. Integration of surface and well data to determine structural controls on permeability at Salak (Awibengkik), Indonesia. *World Geothermal Congress*, (April):25–29, 2010.

[34] J. Stimac, G. Nordquist, A. Suminar, and L. Sirad-Azwar. An overview of the Awibengkok geothermal system, Indonesia. *Geothermics*, 37(3):300–331, 2008.

[35] G. Swan. Determination of Stiffness and Other Joint Properties from Roughness Measurements. *Rock Mechanics and Rock Engineering*, pages 19–38, 1983.

[36] J. Taron, S. Hickman, S. E. Ingebritsen, and C. Williams. Using a fully coupled , open-source THM simulator to examine the role of thermal stresses in shear stimulation of enhanced geothermal systems. *48th US Rock Mechanics / Geomechanics Symposium*, (December 2015), 2014.

[37] N. Tenma, T. Yamaguchi, and G. Zyvoloski. The Hijiori Hot Dry Rock test site, Japan. Evaluation and optimization of heat extraction from a two-layered reservoir. *Geothermics*, 37(1):19–52, 2008.

[38] J. B. Walsh and M. A. Grosenbaugh. A New Model for Analyzing the Effect of Fractures on Compressibility. *Journal of Geophysical Research*, 84:3532–3536, 1979.

[39] D. A. S. Wibowo, G. A. Nordquist, J. Stimac, and A. Suminar. Monitoring Microseismicity during Well Stimulation at the Salak Geothermal Field , Indonesia. (April):25–29, 2010.

[40] K. Yoshioka, B. Izgec, and R. Pasikki. Optimization of Geothermal Well Stimulation Design Using a Geochemical Reservoir Simulator. *33rd Workshop on Geothermal Reservoir Engineering*, pages 1–9, 2008.

[41] J. Zhang, W. B. Standifird, J. C. Roegiers, and Y. Zhang. Stress-dependent fluid flow and permeability in fractured media: From lab experiments to engineering applications. *Rock Mechanics and Rock Engineering*, 40(1):3–21, 2007.

[42] X. Zhang, D. J. Sanderson, R. M. Harkness, and N. C. Last. Evaluation of the 2-D permeability tensor for fractured rock masses. *International Journal of Rock Mechanics and Mining Sciences and Geomechanics*, 33(1):17–37, 1996.

[43] G. A. Zyvoloski. Reservoir modeling of the Phase II Hot Dry Rock system. In *Geothermal Resources Council*, 1984.